Earth and Planetary Science Letters 398 (2014) 48–57

Contents lists available at ScienceDirect

Earth and Planetary Science Letters

www.elsevier.com/locate/epsl

Crustal structure beneath NE China imaged by NECESSArray receiver function data

Kai Tao [a,b,c], Fenglin Niu [b,c,*], Jieyuan Ning [a], Yongshun J. Chen [a], Steve Grand [d], Hitoshi Kawakatsu [e], Satoru Tanaka [f], Masayuki Obayashi [f], James Ni [g]

[a] Institute of Theoretical and Applied Geophysics, Peking University, Beijing, China
[b] State Key Laboratory of Petroleum Resource and Prospecting, and Unconventional Natural Gas Institute, China University of Petroleum at Beijing, Beijing, China
[c] Department of Earth Science, Rice University, Houston, TX, USA
[d] Department of Geological Sciences, The University of Texas at Austin, Austin, TX, USA
[e] Earthquake Research Institute, The University of Tokyo, Tokyo, Japan
[f] Institute for Frontier Research on Earth and Evolution, Japan Agency for Marine–Earth Science and Technology, Yokosuka, Japan
[g] Department of Physics, New Mexico State University, Las Cruces, USA

ARTICLE INFO

Article history:
Received 6 March 2014
Received in revised form 24 April 2014
Accepted 25 April 2014
Available online xxxx
Editor: P. Shearer

Keywords:
northeast China
Songliao basin
residual topography
receiver function
Moho depth

ABSTRACT

We analyzed tens of thousands of receiver-function data recorded by 185 broadband seismic stations to study the crustal structure beneath the northeast China. Moho depth and average crustal Vp/Vs ratio were measured at each station using the H–κ grid searching technique. For stations located above unconsolidated sediments, we applied the H–β method to remove strong shallow reverberations and generate subsurface receiver functions that allow for effective H–κ analysis. The measurements show that the Songliao basin has a relatively thin crust (∼31 km), and the Moho depth increases significantly from southeast (∼27 km) to northwest (∼35 km). The northwestward tilting of the Songliao basin may suggest that it was initiated by lithospheric flexure due to the load of the Great Xing'an range in the Jurassic before the large-scale extension in the Cretaceous. Moho depth varies from 26.7 km to 42.3 km across the study area, with the shallowest and deepest Moho being located at the eastern flank of the Songliao basin and the Great Xing'an range, respectively. The Moho depth correlates well with the surface topography in the western part, but not the central and eastern parts of the study area. The residual topography computed based on the Airy's isostasy model indicates that the high topography at the eastern flank of the Songliao basin, the Changbaishan volcanic center, and the southern end of the Great Xing'an range is likely dynamically supported by the upper mantle.

1. Introduction

The northeast China consists of the northeast China plain (Songliao basin) in its center, the Great Xing'an range to the west, the Changbaishan mountain range and Zhangguangcai range to the east (Fig. 1). The region is bounded by the Sino–Korean craton (also known as the North China craton) in the south at the Solonker suture zone where the paleo-Asian ocean closed at the end of Permian or early Triassic (Chen et al., 2000; Shi et al., 2004). To the north, it is bounded by the Siberian craton at the Mongol–Okhotsk suture (Fig. 1 inset) where the Mongol–Okhotsk Ocean closed progressively from west to east between the middle and late Jurassic (e.g., Meng, 2003; Kravchinsky et al., 2005).

During the later Jurassic and Cretaceous, northeast China experienced large-scale crustal extension and extensive volcanism (Meng et al., 2003), leading to the formation of the Songliao basin and its surrounding volcanic mountains. The cause of the crustal extension and volcanism has been extensively studied and no consensus has been reached. The westward subduction and eastward rollback of the paleo-Pacific plate have been proposed to cause the observed widespread extension and volcanism (Watson et al., 1987; Davis et al., 2004; Ren et al., 2002). On the other hand, several studies (Gao et al., 2004; Wang et al., 2006; Li et al., 2012) suggested that the Cretaceous rifting is likely related to the progressive west to east closure of the Mongol–Okhotsk Ocean. The post-closure collision led to lithospheric thickening of northeast China, and the later collapse of the thickened lithosphere caused convective thinning of the thermal boundary layer

* Corresponding author at: State Key Laboratory of Petroleum Resource and Prospecting, and Unconventional Natural Gas Institute, China University of Petroleum at Beijing, Beijing, China.
E-mail address: niu@rice.edu (F. Niu).

http://dx.doi.org/10.1016/j.epsl.2014.04.043
0012-821X/

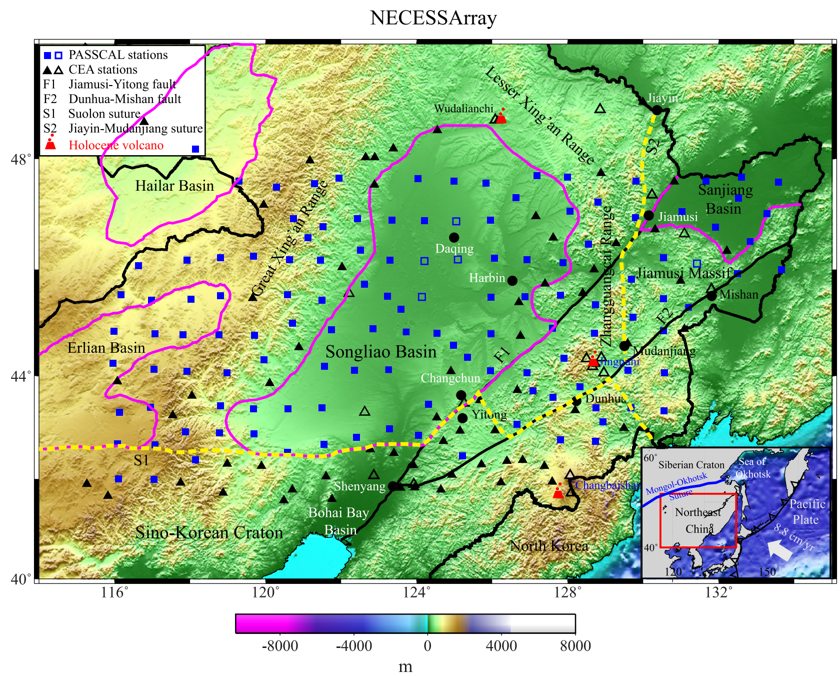

Fig. 1. Map showing topography, major geological features and the distribution of the broadband stations in the northeast China. The purple lines outline major basins in the area. The black solid lines and the dashed yellow lines represent the large strike-slip faults and major suture zones, respectively. The blue squares and black triangles indicate NECESSArray and CEA stations. Solid and open symbols represent the stations with and without (H, κ) measurements, respectively. Red volcanic symbols show the three magmatic centers in the area, Wudalianchi, Jingpohu, and Changbaishan, among which Changbaishan is the largest active magmatic center in China. Solid circles indicate major cities in the area. The bottom-right insect shows the motion of the Pacific plate relative to the Eurasia plate, and the upper-left insect illustrates the legend. (For interpretation of the references to color in this figure legend, the reader is referred to the web version of this article.)

(Molnar et al., 1998; Wang et al., 2006). In addition, gravitational collapse of the thickened and thermally weakened crust could also lead to the generation of rift basins. To understand the dynamics of this region, comprehensive knowledge of crustal structure of the northeast China is needed.

Traveltime tomography has been conducted to study the upper mantle structures beneath eastern Asia (e.g., Huang and Zhao, 2006; Li and van der Hilst, 2010). The tomographic images indicate a slow velocity anomaly beneath the Changbaishan volcanic complex, which has been interpreted as the mantle upwelling that feeds the volcanism. Sun and Toksoz (2006) inverted the P-wave arrival times from the Annual Bulletin of Chinese Earthquakes (ABCE) and developed a 3D P-wave velocity model of the crust and uppermost mantle (up to 120 km deep) beneath China. Receiver function studies using the regional seismic networks operated by the China Earthquake Administration (CEA) have also been conducted to study crustal structure beneath northeast China (Liu and Niu, 2011; Li et al., 2014). In general, station coverage of the CEA regional networks in northeast China is sparse and also extremely uneven. There are only few stations in the eastern side of the Songliao basin, and no CEA stations exist in the central and western parts of the Songliao basin (Fig. 1). Thus the crustal and upper-mantle velocity structure beneath the Songliao basin was poorly constrained by previous seismic studies due to the lack of seismic stations inside the basin.

This study is part of the international collaborative project, NECESSArray (the NorthEast China Extended SeiSmic Array), which deployed a total of 127 portable broadband seismographs in northeast China. The goal of the project is to build high-resolution seismic images of the crust and mantle beneath northeast China to better constrain the subduction geometry of the Pacific plate and to better understand the large-scale extension and widespread magmatism in the area. In particular, we employed the receiver function technique to measure Moho depth and average Vp/Vs ratio at each station. We found that teleseismic recordings at stations inside the Songliao basin and other basins usually exhibit strong sediment reverberations after the direct P arrival, making it nearly impossible to utilize receiver function techniques (Cassidy, 1992; Sheehan et al., 1995; Zelt and Ellis, 1998). For these stations, we applied the H–β analysis developed by Tao et al. (2014), which provides an effective way to remove the shallow reverberations by downward propagating the surface wavefield to the top of the bedrock, leading to better measurements of crustal structure. Our main goal is to present a crustal thickness model of the area as a constraint for ongoing geological and geodynamical studies. An accurate crustal model is also essential to determine the deep lithosphere and mantle structures.

2. Data and analysis

2.1. NECESSArray

We used the waveform data recorded by the NECESSArray, which consists of 127 temporary (blue squares in Fig. 1) and ∼82 permanent broadband stations (black triangles in Fig. 1). The 127 temporal stations were deployed under an international collaboration among China, Japan and US in northeast China between September of 2009 and August of 2011. The permanent stations belong to 6 provincial networks (Beijing, Hebei, Liaoning, Inner Mongolia, Jilin, and Helongjiang provinces) of the China Earthquake Administration (CEA) in the study area (Zheng et al., 2009). The array covers an area of 116°–134° east and 41.5°–49.0° north, roughly ∼1800 km and ∼800 km in the EW and NS direction, respectively (Fig. 1). The average station spacing is ∼80 km, which is still too coarse to apply modern array processing techniques, such as common-conversion-point gathering and pre-stack depth migration, to image the Moho. Thus we employed the single station stacking technique to extract the crustal structure around each station.

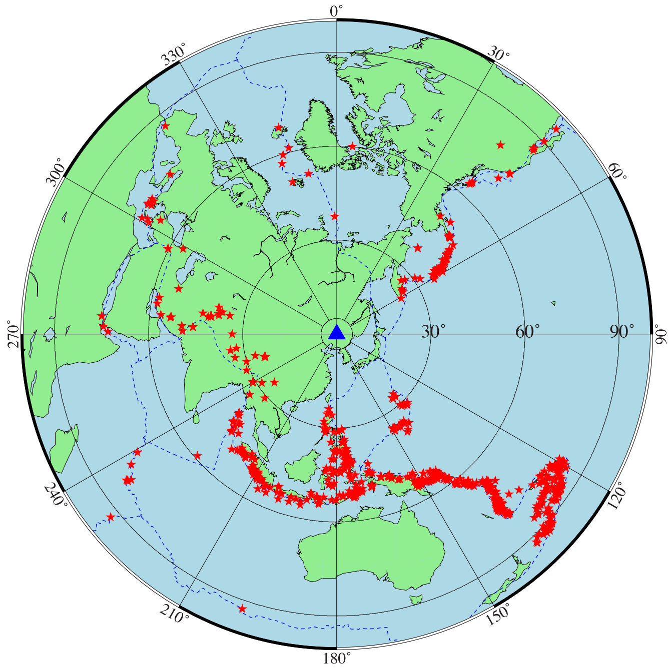

Fig. 2. Distribution of the 788 earthquakes (red stars) used in this study. The blue triangle indicates the center of the seismic array. (For interpretation of the references to color in this figure legend, the reader is referred to the web version of this article.)

We visually examined seismograms of earthquakes with a magnitude greater than 5.0 and in the epicentral distance range of 30°–90° recorded between September of 2009 and August of 2011 by the temporal stations and between July of 2007 and July of 2010 by the CEA stations. We chose a total of 788 earthquakes that are well recorded by the temporal and CEA stations. These earthquakes provide a reasonably good coverage in both distance and azimuthal directions (Fig. 2).

2.2. Receiver functions

We first rotated the two horizontal components of the 3-component seismograms into the radial and transverse components. Niu and Li (2011) found a significant portion of the CEA stations had problems in sensor orientation. We used their estimates of component azimuths, which were determined from P-wave particle motions, to rotate the seismic records of the CEA stations. We further projected the radial and vertical components to the principal directions (longitudinal and in-plane transverse) of the covariance matrix computed from the P-wave data. The receiver functions were then computed from the data projected into this coordinate system (hereafter referred to as P- and SV-component) (Vinnik, 1977; Niu and Kawakatsu, 1998; Niu et al., 2005).

We employed the "water-level" deconvolution technique (Clayton and Wiggins, 1976; Ammon, 1991) to generate receiver functions by a division in frequency domain:

$$RF(\omega) = \frac{V(\omega) \times P^*(\omega)}{\max\{|P(\omega)|^2, k \times |P_{\max}(\omega)|^2\}} e^{-(\frac{\omega}{2a})^2}. \quad (1)$$

Here k and a are two constants that define the "water level" and the corner frequency of the Gaussian low pass filter. k was set to 0.01 and a was set to 1.5, which is equivalent to a corner frequency of ~0.5 Hz. $P(w)$ and $V(w)$ are the spectra of the P and SV components. We used a 60 s time window (5 s before and 55 s after the P wave) for $M \leqslant 7.0$ earthquakes and a 100 s time window (5 s before and 95 s after the P wave) for earthquakes with a magnitude greater than 7. Using the similar way of deconvolution, we also generate receiver functions with the radial and vertical components. We first visually inspected all the receiver functions and removed those with low SNR. At each station, we further calculated the covariance matrix of all the receiver functions and discarded those that showed a low cross correlation coefficient (<0.7) with other traces (Chen et al., 2010). The total number of receiver functions used in the final analysis is 35 527. The number of receiver functions selected for each stations varies from 8 to 315, with an average of ~160. Among the 185 stations that have robust measurements, 171 stations have more than 30 good quality receiver functions.

An example of the receiver functions, which are generated with the P- and SV-components, is shown in Fig. 3a–b. There are two positive pulses after the direct P wave at ~ 4.4 s and 14.8 s, which are expected to be Moho P-to-S conversion phase and the first crustal multiple, 2p1s (Niu and James, 2002). Based on their ray paths, these two phases are expected to have a slightly lower and higher ray parameter (horizontal slowness) than the direct P wave, respectively. In order to determine the relative slowness of these two arrivals and other later phases with respect to the direct P wave, we computed the vespagram of the two sets of receiver functions. To do so, we stacked the receiver functions with linear moveout corrections corresponding to a range of slownesses (e.g., Kawakatsu and Niu, 1994). There are a total of three clear later arrivals shown in the stacked receiver functions. The first later arrival has a slightly negative relative slowness, while the second and third arrivals show positive relative slowness (Fig. 3c–d), indicating that they are the Moho Ps conversion phase and two Moho reverberations, respectively.

2.3. Depth stacking and H–κ analysis

Following Niu et al. (2007), we took two steps to determine the Moho depth and the average Vp/Vs ratio (κ) of the crust beneath a station. Moho depths are referred from the mean sea level and are computed by subtracting station elevations from the measured crustal thickness. We first used a depth-gathering method to determine an initial depth of the Moho beneath a station. Then we employed a refined H–κ analysis to determine the final estimates of depth and Vp/Vs that best explain the observed P to S conversion and the reverberation phases. To obtain the initial depth, we first gathered receiver functions recorded at each station and made a time to depth conversion by assuming that P-to-S conversions are the primary sources of energy in the P-wave coda window. For a conversion depth, d, we first computed the relative arrival time of the converted phase, Pds, with respect to the direct arrival by ray tracing the two phases using a modified 1D iasp91 velocity model (Kennett and Engdahl, 1991), which has a lower crust extending to depth d. We then summed the receiver function values averaged in a 0.1 s window centered on the arrival time of *Pds* using both linear and non-linear stacking technique (e.g., Muirhead, 1968; Kawakatsu and Niu, 1994). We varied d from 0 to 100 km at an increment of 1 km and used the depth with maximum stacking amplitude as the Moho depth. The stacked depth profile at station YA.NE86 is shown in Fig. 4a, which exhibits a clear P-to-S conversion peak at the depth of 35 km.

The crustal thickness, H, estimated with the above depth gathering method depends on the reference velocity model. There is a strong trade off between H and the Vp/Vs ratio or Vp (Nair et al., 2006). Adding the two crustal multiples (2p1s and 1p2s, Niu and James, 2002) in the stacking can, in principle, resolve the trade off (Zhu and Kanamori, 2000). In most of studies, however, the two multiples are assigned a low weight in the stacking due to the low SNR of the two phases. This can introduce large trade off between

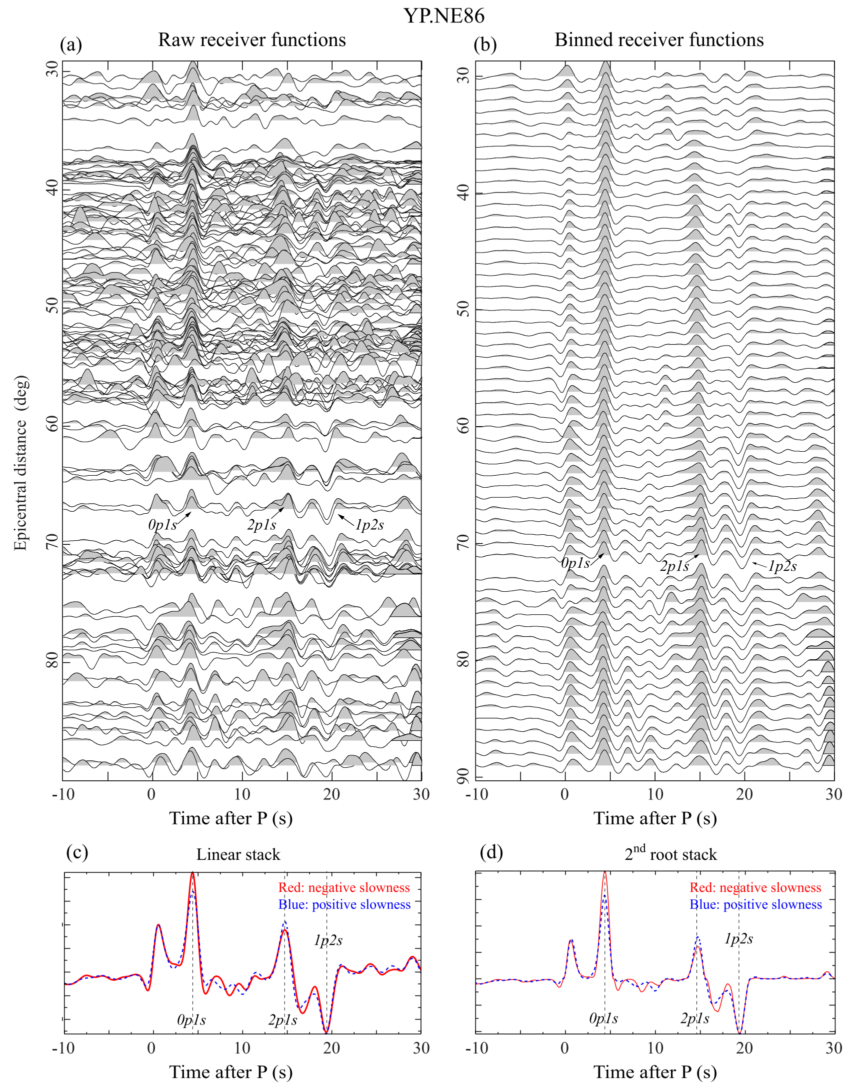

Fig. 3. (a) An example of the individual SV/P receiver functions recorded at station YP.NE86 located in the Great Xing'an range, plotted as a function of epicentral distance. (b) The receiver functions shown in (a) are stacked in 5° bins with increment of 1°. (c) The linearly stacked receiver functions with the Ps slowness (red solid line) and the 2p1s slowness (blue dotted lines). Vertical dashed lines indicate the Ps, 2p1s and 1p2s phase, respectively. (d) Same as (c) except for the stacking method, which is a 2nd-root stack. (For interpretation of the references to color in this figure legend, the reader is referred to the web version of this article.)

H and κ. Niu et al. (2007) introduced a coherence index of the three phases, $c(\kappa)$, which is computed from the cross correlations between depth traces, to reduce the H–κ tradeoff:

$$s(H,\kappa) = \frac{c(\kappa)}{N}\sum_{i=1}^{N}\left\{w_1 r_i(t_i) + w_2 r_i(t_2) - w_3 r_i(t_3)\right\}. \quad (2)$$

Here N is the number of receiver functions at a given station and $r_i(t)$ represents the amplitude of the ith receiver function at the predicted arrival times of the primary P-to-S converted phase $0p1s(t_1)$, and the two crustal multiples, $2p1s(t_2)$ and $1p2s(t_3)$. w_1, w_2, and w_3 are the weights of the three phases, which are assigned to 0.5, 0.25, and 0.25, respectively. We searched for H within ± 20 km of the initial depth determined from the above depth gathering with a step of 0.1 km. κ was varied in the range of 1.5 to 2 with an increment of 0.001. H and κ were finally determined by picking the location where the summed amplitude, $s(H,\kappa)$, reached its maximum. For each station, we used a 1D P-wave velocity model derived from a 3D traveltime tomography study by Sun and Toksoz (2006). The H–κ stacking result at YP.NE86 is shown in Fig. 4b, which exhibits a well-defined peak at $H = 36.4$ km and $\kappa = 1.717$.

2.4. H–β analysis for basin stations

In general, our H–κ analysis technique worked well at most of the stations in northeast China. As an example shown in Figs. 3 and 4, the Moho P-to-S conversion and at least one of the two reverberation phases can be clearly observed on the stacked receiver functions, leading to a well-defined peak in the H–κ diagram. However, the H–κ analysis failed at a number of stations that were located inside the Songliao, Erlian, and Sanjiang basins. The receiver functions generated at these stations had very strong shallow reverberations after the direct P arrival, resulting in multiple peaks in the H–κ domain (Fig. 5). As stated before, the strong sediment reverberations have been always the barriers to implementing receiver-function techniques. For these stations we applied the H–β technique (Tao et al., 2014) that we developed recently to estimate sediment thickness, as well as crustal structure.

Here we briefly review the method proposed by Tao et al. (2014) to estimate sediment and crustal structures beneath a seismic station, which is based on wavefield downward continuation and decomposition. The method parameterizes velocity structure beneath the station with a stack of constant velocity layers overlying a homogeneous half space, and approximates the teleseismic

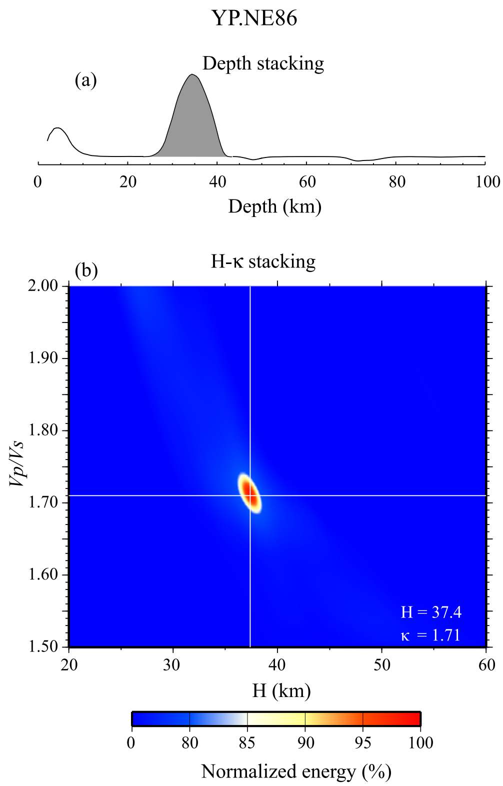

Fig. 4. (a) The stacked receiver function after the time-to-depth conversion at station YP.NE86. The peak of the Ps conversion is at 35 km. (b) Results of the H–κ analysis obtained from YP.NE86. Color shows the summed amplitude as a function of crustal thickness and Vp/Vs ratio. The two white lines indicate location of the amplitude peak. (For interpretation of the references to color in this figure legend, the reader is referred to the web version of this article.)

P-wave and its coda by structural response of an incoming plane P wave. It is based on the principle that the upgoing S wavefield is absent in the half space, and searches for the optimum velocity and thickness of the layers that give the minimum S-wave energy flux from the half space to the layers, which is implemented in an iteratively grid search.

More specifically, we assumed that the crust in the basin consists of two homogeneous layers: an unconsolidated sediment layer and the underlying crystalline crust. We assumed that the P-wave velocity and density are known, which are (2.1 km/s, 1.97 g/cm^3) for the sediment, and (6.4 km/s, 2.7 g/cm^3) for the crust. The half-space mantle has a seismic structure of 8.0 km/s, 4.5 km/s, and 3.3 g/cm^3 for P-, S-wave velocity, and density, respectively. We only searched the thickness and S-wave velocity of the sediment and hard-rock crust to minimize upgoing S wave energy fluxing from the half-space mantle to the crust. An example of the H–β searching result at the YP.NEA5 station is plotted in Fig. 6a–b, which shows that the final estimates of the thickness and S-wave velocity of the sediment and underlying crust are (0.59 km, 0.61 km/s) and (31.6 km, 3.67 km/s), respectively.

We further applied the wavefield downward-continuation technique to propagate the surface records to the top of the crystalline crust, and then formed subsurface receiver functions by deconvolving the upgoing P wave from upgoing S waves at the top of the crust (Fig. 6c–d). In principle the wavefield at the top of the crust is not contaminated by sediment multiples. This is demonstrated by comparing the subsurface receiver functions in Fig. 6c–d with those of the regular receiver functions (Fig. 5a–b). While the surface receiver functions are dominated by large-amplitude shallow reverberations that completely mask out the Moho related arrivals (Fig. 5a–b), the Moho P-to-S conversion and the 2p1s multiple can actually be recognized from the subsurface receiver functions in Fig. 6c–d. Also the H–κ stacking of the sub-surface receiver functions yielded a well-defined peak in the H–κ domain (Fig. 6g). The estimated crustal thickness and Vp/Vs ratio based on the H–κ analysis of the subsurface receiver functions are consistent with the H–β results.

3. Results and discussion

3.1. Crustal thickness and Vp/Vs ratio

Among the 209 stations, we were able to obtain 185 measurements of Moho depth and Vp/Vs ratio including 18 H–β measurements (solid squares and triangles in Fig. 1). The other 24 stations either suffered malfunctions or recorded very noisy data (open squares and triangles in Fig. 1). The results are listed in Table S1. The table is organized by grouping stations in the following tectonic/physiographic regions: the Songliao basin (SLB), the Great Xing'an range (GXA), the Erlian basin (ELB), the Hailar basin (HLB), the Zhangguangcai range (ZGC), the Sanjiang basin (SJB), the Jiamusi Massif (JMS), and northern edge of the Sino–Korea craton (SKC). In Table S1, we also showed 1σ errors, which were calculated based on a bootstrap method (Efron and Tibshirani, 1986). We note that these are formal errors, which do not include uncertainty in the velocity model, and actual errors are likely higher. As shown by previous studies, κ is almost insensitive to the reference Vp model while H depends monotonically on the assumed Vp value. Chen et al. (2010) found that the model-induced uncertainty in Moho depth is expected to be <6–8%.

The measured crustal thickness shows significant variations across the study area, varying from 26.9 km to 43.5 km with an average of 34.0 km. The shallowest Moho is observed at YP.NE59 at the central eastern edge of the Songliao basin, while the thickest crust is located beneath the station YP.NE52 in the central part of the Great Xing'an range (Fig. 1 and Table S1). The observed crustal thickness roughly shows a positive correlation with surface topography (Fig. 7a), and this correlation appears to hold only in the Great Xing'an range. The observed crustal thickness seems to have no correlation with the observed the Vp/Vs ratio (Fig. 7b), which varies between 1.616 and 1.869 with an average of 1.748. In the following sections, we first show the maps of Moho topography and Vp/Vs ratio through interpolation of the 185 observations in order to better exhibit lateral variations of the two parameters. We further divide the study area into western, central and eastern parts and describe the major features of the crust structure observed in these subareas, with a discussion on their tectonic and dynamic implications.

Following Niu et al. (2007), we employed an inversion method to interpolate the 185 measurements and generate 2D relief maps for Moho depth and Vp/Vs ratio, respectively (Fig. 8). More specifically, we divided the study area from 42.0°N to 49°N (latitude) and 116°E to 132°E (longitude) into meshed grids of 0.25° × 0.25°. The total 1885 (29 × 65) unknown parameters of Moho depth were inverted from 185 observations. The kernel matrix has a dimension of 185 × 1885 with 185 non-zero elements (= 1) that correspond to the 185 observations. A regularization that minimizes the first derivative of the model (the flattest Moho) was added to regularize the underdetermined inversion. Details of this algorithm were described in Niu et al. (2007). We must note here that the main purpose for generating the 2D maps is to demonstrate lateral variations in Moho depth and Vp/Vs ratio across the study area. The actual resolution is probably not as high as the 0.25° × 0.25° grid spacing. Moreover, our data have no resolution in the corner regions, which are not shown in Fig. 8.

The thickest crust is found in the western part of the study area, i.e., the Great Xing'an range, the Erlian and Hailar basins. This

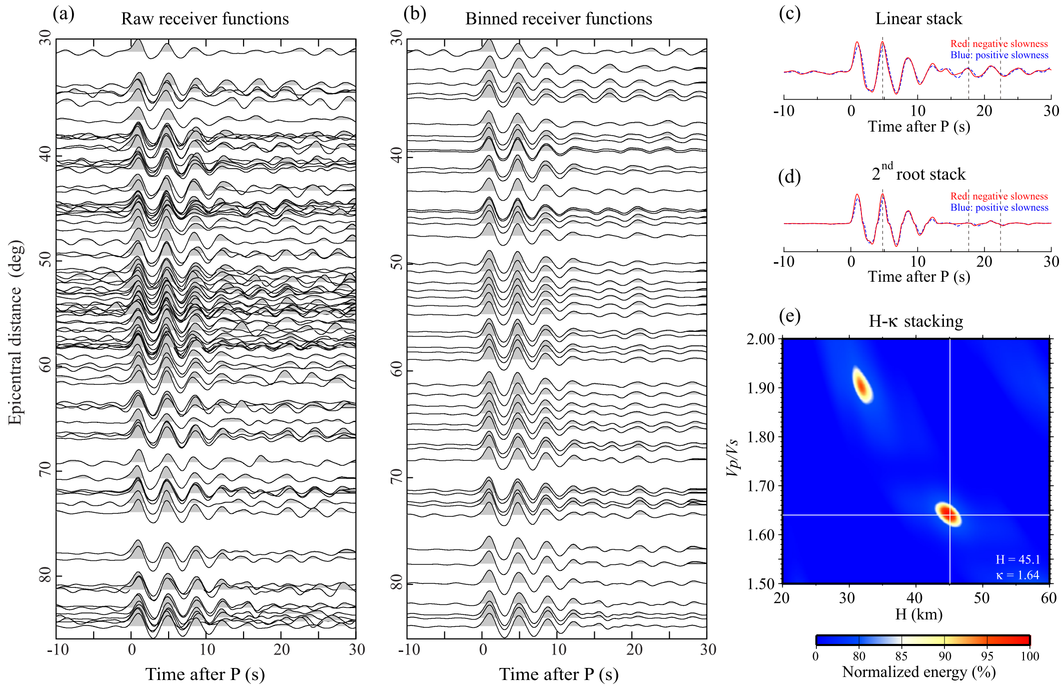

Fig. 5. (a) The individual receiver functions generated at the station YP.NEA5 located in the northern Songliao basin, plotted as a function of epicentral distance. Note the large reverberations from the base of the sediments. (b) The receiver functions shown in (a) are stacked in 5° bins with increment of 1°. (c) The linearly stacked receiver functions with the Ps slowness (red solid line) and the 2p1s slowness (blue dotted lines). Vertical dashed lines indicate the Ps, 2p1s and 1p2s phase, respectively. (d) Same as (c) except for the stacking method, which is a 2nd-root stack. (e) Results of the H–κ analysis obtained from YP.NEA5. Color contours show the summed amplitude as a function of crustal thickness and Vp/Vs ratio. The two white lines indicate location of the amplitude peak. Note that multiple peaks exist in the (H, κ) domain. (For interpretation of the references to color in this figure legend, the reader is referred to the web version of this article.)

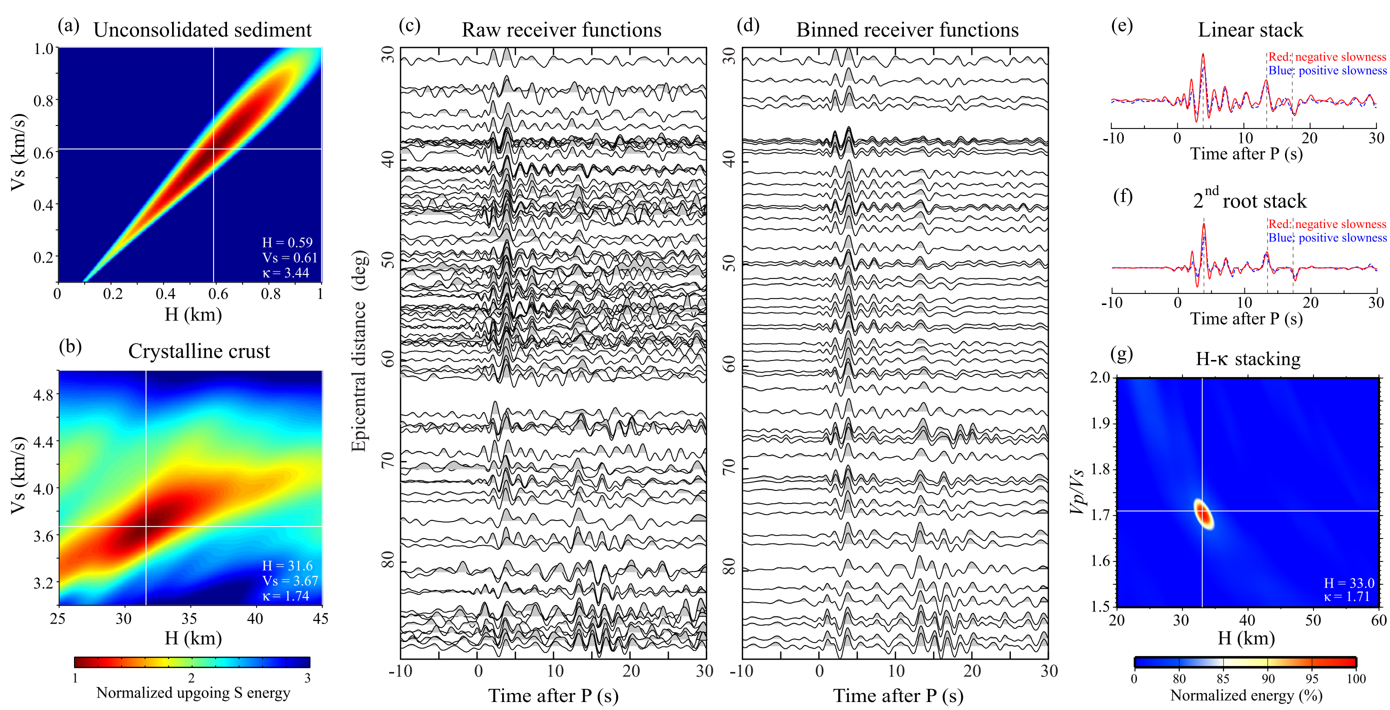

Fig. 6. The H–β search results, sub-surface receiver functions and the H–κ stacking of the sub-surface receiver functions of the station YP.NEA5 shown in Fig. 5. Results of the H–β search on the thickness and S-wave velocity of the unconsolidated sediment layer and the underlying crystalline crust are shown in (a) and (b), respectively. Color shows the upgoing S-wave energy normalized by its minimum value as a function of layer thickness and average S-wave velocity. (c) The subsurface receiver functions are computed through downward propagating the surface wavefield to the top of the crystalline crust. Note that the strong reverberations shown in Fig. 5a are largely suppressed. (d) The receiver functions shown in (a) are stacked in 5° bins with increment of 1°. (e) The linearly stacked receiver functions with the Ps slowness (red solid line) and the 2p1s slowness (blue dotted lines). Vertical dashed lines indicate the Ps, 2p1s and 1p2s phase, respectively. (f) Same as (e) except for the stacking method, which is a 2nd-root stack. (g) Results of the H–κ analysis obtained from the subsurface receiver functions shown in (c). Color shows the summed amplitude as a function of crustal thickness and Vp/Vs ratio. The two white lines indicate location of the amplitude peak. (For interpretation of the references to color in this figure legend, the reader is referred to the web version of this article.)

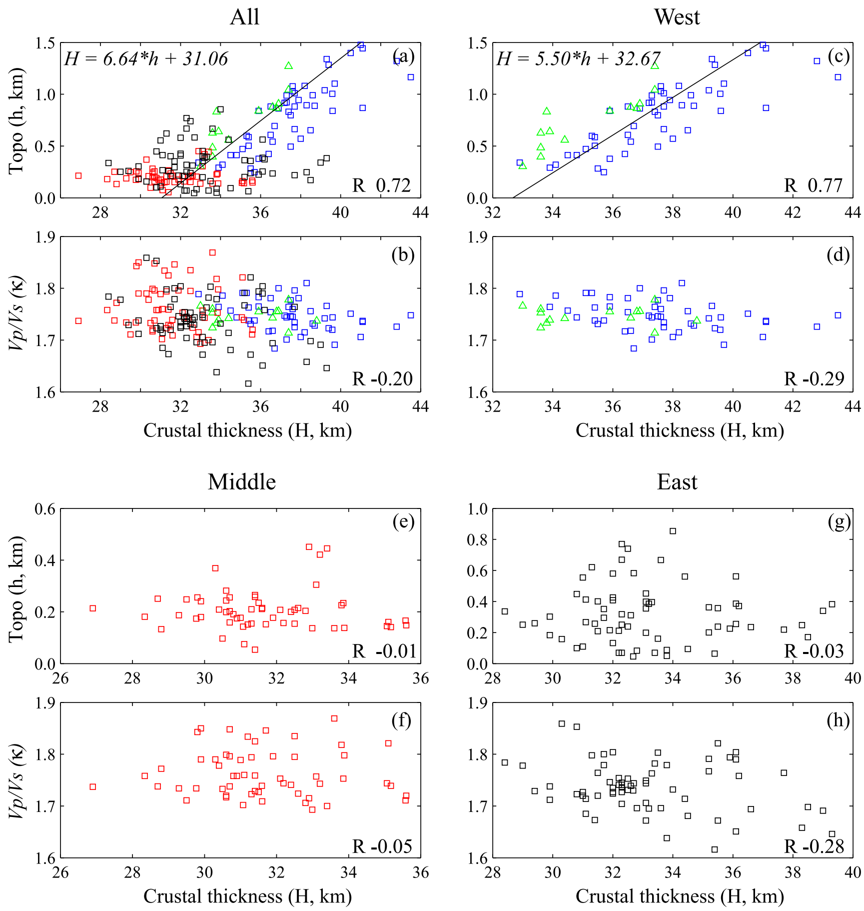

Fig. 7. Relationship among surface topography, crustal thickness, and Vp/Vs. The correlation coefficients are indicated in the bottom-right of each plot. (a) and (b) show the surface topography and Vp/Vs ratio as a function of the crustal thickness, respectively, based on all the 185 measurements. Blue and green symbols indicate measurements from stations located in the west part of the study area, including the Great Xing'an range, the Erlian basin and the Hailar basin. Red and black represent measurements from the central and eastern areas. The estimated crustal thickness generally shows a positive correlation with surface topography but no correlation with Vp/Vs ratio. Similar plots of the western, central and eastern areas are shown in (c, d), (e, f) and (b, d), respectively. Note that the positive correlation between surface topography and crustal thickness is only clearly shown in the western area, and there is no clear correlation between Vp/Vs ratio and crustal thickness in all the three regions. The green triangles shown in (a) and (c) indicate stations located at the southern end of the Great Xing'an range, which have elevations higher than those predicted by the Airy isostasy model. (For interpretation of the references to color in this figure legend, the reader is referred to the web version of this article.)

part of the area has a topography varying from 0.25 to 1.52 km with an average of 0.81 km. The Moho is located between 32.6 and 42.3 km deep below the mean sea level, with an average depth of 36.3 km. There is a clear positive correlation between the crustal thickness and station elevation (Fig. 7c), suggesting that most of the surface topography is supported by a deep crustal root. On the other hand, the Vp/Vs ratio appears to have no distinct correlation with the observed crustal thickness (Fig. 7d). The regional average of the Vp/Vs ratio is 1.748, very close to the average of the whole study area.

The Songliao basin in the middle of the study area is underlain by a thin to moderately thick crust, with thickness varying from 26.9 km to 35.6 km and an average of 31.7 km. The shallowest Moho is observed beneath the eastern edge of the basin at the conjunction with the Zhangguangcai range, while the deepest Moho is located in the northwest corner. The northern Songliao basin (with a latitude higher than 45°N) appears to have a slightly thicker crust (∼33.2 km) than its southern neighbor (∼32.4 km) (Fig. 8a). The post-rift sediment is well developed in the northern Songliao basin, which can reach as thick as 4 km, while the post-rift sediment is found to be less than 1 km in the southern area (Wei et al., 2010). This difference may explain the observed crustal thickness between the northern and southern Songliao basin. Surface topography inside the basin varies from 0.054 km in the west to 0.451 km in the east, with an average of ∼0.206 km. There is no obvious correlation between the observed crustal thickness and the surface topography (Fig. 7e), suggesting that the surface topography is balanced by something different from the Airy isostasy model. The average Vp/Vs ratio of the Songliao basin is ∼1.763, which is slightly higher than the average of the whole study area. In general, the presence of thick sediments can increase Poisson's ratio, which is likely the cause for the observed high Vp/Vs ratio, since most of the Vp/Vs ratio measurements inside the basin are based on the H–κ analysis, which is averaged over the entire crust including the sediments.

The eastern part of the area consists of the northeastern edge of the Sino–Korea craton, the Zhangguangcai range, the Jiamusi Massif and the Sanjiang basin. We observed a large depth variation of the Moho in this area, from 28.4 km to 39.3 km. The thin crust is located beneath the northeastern Sino–Korea craton southeast to the Songliao basin, western part of the Zhangguangcai range, as well as the Sanjiang basin, while the eastern side of the Zhangguangcai range and the Jiamusi Massif are underlain by a relatively thick crust. The Sanjiang basin has a relatively high Vp/Vs ratio, partly because of the infilling sediments, which usually have very high Vp/Vs ratio. There is no obvious correlation between the observed crustal thickness and surface topography or Vp/Vs ratio (Fig. 7g–h).

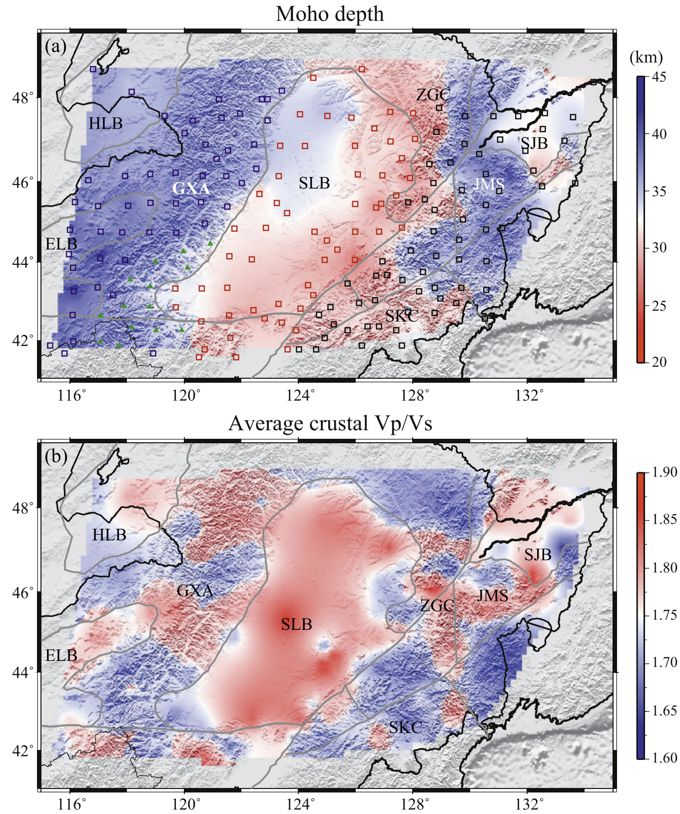

Fig. 8. (a) Moho relief map inverted from observations at stations shown as solid triangles and open squares. An inversion was performed to minimize the lateral variation of Moho depth (see Niu et al., 2007 for details). Note the gradual increase of Moho depth from southeast to northwest across the Songliao basin. Colors correspond to the three different regions shown in Fig. 7. The green triangles at the southern end of the Great Xing'an range indicate the region with positive topographic residual as shown in Fig. 9. (b) Map of lateral variations for the Vp/Vs ratio. The same inversion method is used for generating the map. Note the Songliao basin in the central area has a slightly high Vp/Vs ratio. Although the maps here were obtained from a regularized inversion, any decent interpolations are expected to yield more or less the same results. (For interpretation of the references to color in this figure legend, the reader is referred to the web version of this article.)

3.2. Residual topography

Using the observed crustal thickness, we further compute the theoretical topography based on the Airy isostasy model:

$$h = \frac{\rho_m - \rho_c}{\rho_m} H - \frac{\rho_m - \rho_c}{\rho_m} H_0 \tag{3}$$

where H is the observed crustal thickness, and h is the expected topography. ρ_c and ρ_m are crustal and mantle density. If we take $\rho_c = 2.67\ \mathrm{g\,cm^{-3}}$, $\rho_m = 3.3\ \mathrm{g\,cm^{-3}}$, and the average crustal thickness $H_0 = 33.6$ km, then Eq. (3) becomes $h = 0.191 * H - 6.414$. Since measurement uncertainty in the crustal thickness is much larger than the surface topography, we thus conducted a L2 linear regression using h as the variable. We obtained $H = 6.64 * h + 31.06$ for the whole area, and $H = 5.50 * h + 32.67$ for the western region, which can be converted, respectively, to

$$h = 0.150 * H - 4.4669 \tag{4a}$$

$$h = 0.182 * H - 5.940. \tag{4b}$$

We used Eq. (4a) to compute the expected topography from the observed crustal thickness at each station. The residual topography at each station is then computed as the difference between the observed and predicted topography. We further employed the same inversion method described above to interpolate the 185 measurements and generated a map of the residual topography of the study area.

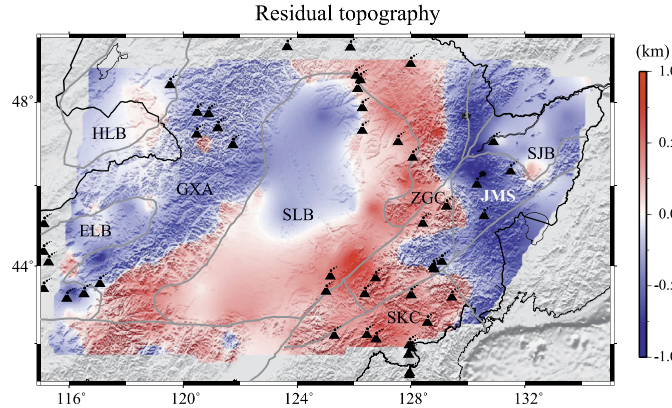

Fig. 9. Map showing the residual topography and locations of Cenozoic volcanism. We used the same inversion method as the Moho relief map shown in Fig. 8a in generating the map. Note that the eastern flank of the Songliao basin, the Changbaishan mountain range, and the southern end of the Great Xing'an range (corresponding to stations indicated by green triangles in Fig. 7) show significant positive topographic residuals, suggesting that the surface topography in these areas is likely supported dynamically by the upper mantle. (For interpretation of the references to color in this figure legend, the reader is referred to the web version of this article.)

Fig. 9 shows the resulting residual topography map, which reveals a lateral variation between −1 and 1 km. Negative topographic residuals are observed in the most part of the Great Xing'an range, the northwestern part of the Songliao basin and the Jiamusi Massif (Fig. 9). The southern part of the Songliao basin shows a slightly positive to zero residual, indicating it is nearly under isostatic equilibrium. On the other hand, large positive residuals are shown at the southern tip of Great Xing'an range, the eastern flank of Songliao basin and the Changbaishan mountain range. It appears that most of the Cenozoic volcanism occurred in these regions with positive topographic residuals (Fig. 9).

Sedimentary stratigraphy studies indicate that the northern and southern parts of the Songliao basin have experienced different tectonic subsidence history. While seismic stratigraphy reveals rather similar syn-rift strata between the northern and southern parts of the basin, the amount of post-rift deposition appears to be significantly different. The post-rift strata within the northern Songliao basin are well developed, indicating a large-magnitude post-rift subsidence. In contrast, the southern Songliao basin exhibits a minor post-rift subsidence despite undergoing intense rifting (Wei et al., 2010). Numerical modeling (McKenzie, 1978) indicates that pure-shear induced rifting is usually accompanied by substantial thermal subsidence after the rifting, which does not seem to occur in the southern Songliao basin. One possible scenario that has been invoked to explain the observation here is the injection of lower crust material to the area, which could have elevated the topography and thus compensate the post-rift thermal subsidence. The ductile lower crustal material can flow from the over-thickened crust beneath the Great Xing'an range (McKenzie et al., 2000; Meng, 2003; Wei et al., 2010). If this is the case, the southern and northern parts of the Songliao basin are expected to have roughly similar Moho depth but different Vp/Vs ratio after taking account for the thick post-rift sediments in the north and the injected lower crust material in the south, which are not observed from the receiver function data. In general, if crustal thickening were accomplished by injection of lower crustal materials, then one would expect to observe a positive correlation between crustal thickness and Vp/Vs ratio, as mafic lower crustal rocks tend to have high Vp/Vs ratios. Our data, however, do not show such a positive correlation.

The average crustal thickness of the Songliao basin is ∼31.7 km, a few kilometers thinner than those observed beneath cratons around the world that experienced little deformations, for example ∼35 km beneath the Kaapvaal and Zimbabwe cratons in Africa (Nguuri et al., 2001) and ∼37 km beneath the Guayana shield in South America (Niu et al., 2007). Lithosphere stretching is believed to be the cause of the thin crust beneath the basin (Lin et al., 1997). Our observations also suggest that the overall thinned crust thickens gradually towards northwest, which is difficult to be explained by a uniform stretching.

The residual topography map (Fig. 9) shows that Songliao basin is surrounded by positive residuals in the east, south and southwest sides, suggesting that the surface topography of the Zhangguangcai range, the Changbaishan mountain range, and the southern end of the Great Xing'an range is likely supported dynamically by mantle upwellings, which are also suggested by other seismic studies such as surface wave tomography, P- and S-wave tomography, and seismic anisotropy (Chen et al., 2012). The upwellings can cause the northwestward tilt of the Songliao basin, resulting in an increase in sediment deposition and crustal thickness towards northwest, which agrees with the observed Moho topography beneath the basin (Fig. 8a). If this is the scenario, then the large scale stretching is expected to occur first, followed by the upwelling event. In other words, the tilt is developed in a later stage after the formation of the basin. Liu et al. (2001) observed a sudden migration of volcanism from the middle part of the Songliao basin to the eastern edge at around 30 Ma. This is consistent with our proposed sequential order of the extension and upwelling events.

Foreland basins are usually developed adjacent and parallel to a mountain belt, because the immense mass created by crustal thickening associated with the evolution of the mountain belt causes the lithosphere to bend, by a process known as lithospheric flexure (Watts, 2001). Another possible explanation for the cause of the northwestward tilting of the Songliao basin thus could be related to lithospheric flexure due to the load of the Great Xing'an range in the west and northwest. The basin formed as a foreland basin, probably in the Jurassic before the large-scale extension occurring in the early Cretaceous. This implies that the Songliao basin experienced a low degree of deformation during the crustal shortening stage associated with the closure of the Mongol–Okhotsk Ocean, probably because of its strong cratonic keel. The large-scale crustal stretching occurring in the Cretaceous was likely caused by backarc extension associated with the westward subduction and eastward rollback of the paleo-Pacific plate.

4. Conclusions

We investigated crustal structure beneath the northeast China using waveform data recorded by 185 broadband seismic stations in the region. The receiver function data revealed the following features of the crust beneath the study area: (1) the crust beneath the Erlian and Hailar basins is much thicker (∼38 km) than that (∼32 km) beneath the Songliao and Sanjiang basins, suggesting they are formed with different mechanism. (2) The southern end of the Great Xing'an range is underlaid by a relatively shallow Moho, indicating that the high surface topography in this area is likely supported dynamically by a mantle upwelling, which is also suggested by other seismic data. (3) The Moho beneath the Songliao basin deepens gradually from southeast to northwest. The northern Songliao basin covered by thick post-rift sediment strata has a slightly thicker crust than the southern Songliao basin. The observed crustal Vp/Vs ratio beneath the Songliao basin is generally higher than the surrounding areas, but shows no significant difference between the southern and northern parts. We speculate that the observed lateral variations in crustal structure beneath the Songliao basin was either developed by mantle upwellings after the rifting or inherited from the initial stage of the formation.

Acknowledgements

We thank all the people involved in the NECESSArray project for installing and servicing the seismic array, the Data Management Center of the China National Seismic Network for providing the CEA waveform data. We also thank two anonymous reviewers for their constructive comments and suggestions, which significantly improved the quality of this paper. K.T., J.N., Y.C. are supported by NSFc, F.N., S.G., and J.N., are supported by NSF under the grant EAR-0635666, EAR-0635855, EAR-0634903, respectively, H.K., S.T., and M.O., are supported by the JSPS grant 19104011.

Appendix A. Supplementary material

Supplementary material related to this article can be found online at http://dx.doi.org/10.1016/j.epsl.2014.04.043.

References

Ammon, C.J., 1991. The isolation of receiver effects from teleseismic P waveforms. Bull. Seismol. Soc. Am. 81, 2504–2510.
Cassidy, J.F., 1992. Numerical experiments in broadband receiver function analysis. Bull. Seismol. Soc. Am. 82, 1453–1474.
Chen, B., Jahn, B.M., Wilde, S., Xu, B., 2000. Two contrasting Paleozoic magmatic belts in northern Inner Mongolia, China. Tectonophysics 328, 157–182. http://dx.doi.org/10.1016/S0040-1951(00)00182-7.
Chen, Y., Niu, F., Liu, R., Huang, Z., Tkalcic, H., Sun, L., Chan, W., 2010. Crustal structure beneath China from receiver function analysis. J. Geophys. Res. 115, B03307. http://dx.doi.org/10.1029/2009JB006386.
Chen, Y.J., Tang, Y., Grand, S.P., Niu, F., Kawakatsu, H., Ning, J., Tanaka, S., Obayashi, M., Ni, J., 2012. Seismic evidence for possible lithospheric drips beneath the Greater Xiang'an Range by NECESSArray. Abstract T41F-06 presented at 2012 Fall Meeting, AGU, San Francisco, Calif., 3–7 Dec.
Clayton, R.W., Wiggins, R.A., 1976. Source shape estimation and deconvolution of teleseismic body waves. Geophys. J. R. Astron. Soc. 47, 151–177.
Davis, G.A., Xu, B., Zheng, Y., Zhang, W., 2004. Indosinian extension in the Solonker suture zone: the Sonid Zuoqi metamorphic core complex, Inner Mongolia, China. Earth Sci. Front. 11 (3), 135–144.
Efron, B., Tibshirani, R., 1986. Bootstrap methods for standard errors, confidence intervals, and other measures of statistical accuracy. Stat. Sci. 1 (1), 54–77.
Gao, S., Rudnick, R.L., Yuan, H.L., 2004. Recycling lower continental crust in the north China craton. Nature 432, 892–897. http://dx.doi.org/10.1038/nature03162.
Huang, J.L., Zhao, D.P., 2006. High-resolution mantle tomography of China and surrounding regions. J. Geophys. Res. 111, B09305. http://dx.doi.org/10.1029/2005JB004066.
Kawakatsu, H., Niu, F., 1994. Seismic evidence for a 920-km discontinuity in the mantle. Nature 371, 301–305.
Kennett, B.L.N., Engdahl, E.R., 1991. Traveltimes for global earthquake location and phase identification. Geophys. J. Int. 105, 429–465. http://dx.doi.org/10.1111/j.1365-246X.1991.tb06724.x.
Kravchinsky, V.A., Halim, N., Hankard, F., 2005. Late Jurassic–Early Cretaceous closure of the Mongol–Okhotsk Ocean demonstrated by new Mesozoic paleomagnetic results from the Trans-Baikal area (SE Siberia). Geophys. J. Int. 163, 813–832. http://dx.doi.org/10.1111/j.1365-246X.2005.02782.x.
Li, C., van der Hilst, R.D., 2010. Structure of the upper mantle and transition zone beneath Southeast Asia from traveltime tomography. J. Geophys. Res. 115, B07308. http://dx.doi.org/10.1029/2009JB006882.
Li, S.Q., Chen, F.K., Siebel, W., Wu, J.D., Zhu, X.Y., Shan, X.L., Sun, X.M., 2012. Late Mesozoic tectonic evolution of the Songliao basin, NE China: evidence from detrital zircon ages and Sr–Nd isotopes. Gondwana Res. 22, 943–955.
Li, Y., Gao, M., Wu, Q., 2014. Crustal thickness map of the Chinese mainland from teleseismic receiver functions. Tectonophysics 611, 51–60.
Lin, C., Li, S., Zhang, Q., Zhang, Y., 1997. Lithosphere stretching, subsidence and thermal history modeling: application to Yinggehai, Qiongdongnan and Songliao basins in east China. J. China Univ. Geosci. 8 (1), 83–89.
Liu, J., Han, J., Fyfe, W.S., 2001. Cenozoic episodic volcanism and continental rifting in northeast China and possible link to Japan Sea development as revealed from K-Ar geochronology. Tectonophysics 339, 385–401.
Liu, H., Niu, F., 2011. Receiver function study of the crustal structure of Northeast China: seismic evidence for a mantle upwelling beneath the eastern flank of the Songliao Basin and the Changbaishan region. Earthq. Sci. 24, 27–33.
McKenzie, D., 1978. Some remarks on the development of sedimentary basins. Earth Planet. Sci. Lett. 40, 25–32. http://dx.doi.org/10.1016/0012-821X(78)90071-7.

McKenzie, D., Nimmo, F., Jackson, J.A., Gans, P.B., Miller, E.L., 2000. Characteristics and consequences of flow in the lower crust. J. Geophys. Res. 105, 11029–11046. http://dx.doi.org/10.1029/1999JB900446.

Meng, Q.R., 2003. What drove late Mesozoic extension of the northern China–Mongolia tract? Tectonophysics 369, 155–174.

Meng, Q.R., Hu, J.M., Jin, J.Q., Zhang, Y., Xu, D.F., 2003. Tectonics of the late Mesozoic wide extensional basin system in the China–Mongolia border region. Basin Res. 15, 397–415.

Molnar, P., Houseman, G.A., Conrad, C.P., 1998. Rayleigh–Taylor instability and convective thinning of mechanically thickened lithosphere: effects of non-linear viscosity decreasing exponentially with depth and of horizontal shortening of the layer. Geophys. J. Int. 133, 568–584.

Muirhead, K.J., 1968. Eliminating false alarms when detecting seismic events automatically. Nature 217, 533–534.

Nair, S.K., Gao, S.S., Liu, K.H., Silver, P.G., 2006. Southern African crustal evolution and composition: constraints from receiver function studies. J. Geophys. Res. 111, B02304. http://dx.doi.org/10.1029/2005JB003802.

Nguuri, T.K., Gore, J., James, D.E., Webb, S.J., Wright, C., Zengeni, T.G., Gwavava, O., Snoke, J.A., 2001. Crustal structure beneath southern Africa and its implications for the formation and evolution of the Kaapvaal and Zimbabwe cratons. Geophys. Res. Lett. 28, 2501–2504.

Niu, F., Kawakatsu, H., 1998. Determination of the absolute depths of the mantle transition zone discontinuities beneath China: effect of stagnant slabs on mantle transition zone discontinuities. Earth Planets Space 50, 965–975.

Niu, F., James, D.E., 2002. Fine structure of the lowermost crust beneath the Kaapvaal craton and its implications for crustal formation and evolution. Earth Planet. Sci. Lett. 200, 121–130. http://dx.doi.org/10.1016/S0012-821X(02)00584-8.

Niu, F., Levander, A., Ham, S., Obayashi, M., 2005. Mapping the subducting Pacific slab beneath southwest Japan with Hi-net receiver functions. Earth Planet. Sci. Lett. 239, 9–17.

Niu, F., Bravo, T., Pavlis, G., Vernon, F., Rendon, H., Bezada, M., Levander, A., 2007. Receiver function study of the crustal structure of the southeastern Caribbean plate boundary and Venezuela. J. Geophys. Res. 112, B11308. http://dx.doi.org/10.1029/2006JB004802.

Niu, F., Li, J., 2011. Component azimuths of the CEArray stations estimated from P wave particle motion. Earthq. Sci. 24, 3–13. http://dx.doi.org/10.1007/s11589-011-0764-8.

Ren, J., Tamaki, K., Li, S., Zhang, J., 2002. Late Mesozoic and Cenozoic rifting and its dynamic setting in eastern China and adjacent areas. Tectonophysics 344, 175–205. http://dx.doi.org/10.1016/S0040-1951(01)00271-2.

Sheehan, A.F., Abers, G.A., Jones, C.H., Lerner-Lam, A.L., 1995. Crustal thickness variations across the Colorado Rocky Mountains from teleseismic receiver functions. J. Geophys. Res. 100, 20391–20404.

Shi, Y., Liu, D., Zhang, Q., 2004. SHRIMP geochronology of dioritic-granitic intrusions in Sunidzuoqi area, Inner Mongolia. Acta Geol. Sin. 78, 789–799 (in Chinese with English abstract).

Sun, Y.S., Toksoz, M.N., 2006. Crustal structure of China and surrounding regions from P wave traveltime tomography. J. Geophys. Res. 111, B03310. http://dx.doi.org/10.1029/2005JB003962.

Tao, K., Liu, T.Z., Ning, J.Y., Niu, F., 2014. Estimating sedimentary and crustal structure using wavefield continuation: theory, techniques and applications. Geophys. J. Int. 197, 443–457. http://dx.doi.org/10.1093/gji/ggt515.

Wang, F., Zhou, X., Zhang, L., Ying, J., Zhang, Y., Wu, F., Zhu, R., 2006. Late Mesozoic volcanism in the Great Xing'an Range (NE China): timing and implications for the dynamic setting of NE Asia. Earth Planet. Sci. Lett. 251, 179–198. http://dx.doi.org/10.1016/j.epsl.2006.09.007.

Watson, M.P., Hayward, A.B., Parkinson, D.N., Zhang, Z.M., 1987. Plate tectonic history, basin development and petroleum source rock deposition onshore China. Mar. Pet. Geol. 4, 205–225. http://dx.doi.org/10.1016/0264-8172(87)90045-6.

Watts, A.B., 2001. Isostasy and Flexure of the Lithosphere. University of Oxford.

Wei, H.H., Liu, J.L., Meng, Q.R., 2010. Structural and sedimentary evolution of the southern Songliao Basin, northeast China, and implications for hydrocarbon prospectivity. Am. Assoc. Pet. Geol. Bull. 94, 533–566.

Vinnik, L.P., 1977. Detection of waves converted from P to SV in the mantle. Phys. Earth Planet. Inter. 15, 39–45.

Zelt, B.C., Ellis, R.M., 1998. Receiver function studies in the Trans-Hudson orogen, Saskatchewan. Can. J. Earth Sci. 36, 585–603.

Zheng, X.F., Ouyang, B., Zhang, D.N., Yao, Z.X., Liang, J.H., Zheng, J., 2009. Technical system construction of Data Backup Centre for China Seismograph Network and the data support to researches on the Wenchuan earthquake. Chin. J. Geophys. 52, 1412–1417. http://dx.doi.org/10.3969/j.issn.0001-5733.2009.05.031 (in Chinese).

Zhu, L., Kanamori, H., 2000. Moho depth variation in southern California from teleseismic receiver functions. J. Geophys. Res. 105, 2969–2980.